

SELECTED TOPICS IN APPLIED PHYSICS

## Strategy to utilize transmission electron microscopy and X-ray diffraction to investigate biaxial strain effect in epitaxial $\text{BiFeO}_3$ films

To cite this article: In-Tae Bae *et al* 2018 *Jpn. J. Appl. Phys.* **57** 0902A5

View the [article online](#) for updates and enhancements.

### You may also like

- [Structure, Defects and Thermal Stability of Delithiated Olivine Phosphates](#)  
Gene M. Nolis, Heng Yang, Natasha A. Chernova *et al.*
- [Studies of Reaction Mechanisms in Nano-Structured Conversion Electrodes Using Magnetic Properties](#)  
Natasha A. Chernova, Ruigang Zhang, Frederick Omenya *et al.*
- [The Optimum Composition of  \$\text{LiNi}\_x\text{Mn}\_y\text{Co}\_{1-x-y}\text{O}\_2\$](#)   
Zheng Li, Natasha A. Chernova, Megan Roppolo *et al.*



## Strategy to utilize transmission electron microscopy and X-ray diffraction to investigate biaxial strain effect in epitaxial BiFeO<sub>3</sub> films

In-Tae Bae<sup>1,2\*</sup>, Tomohiro Ichinose<sup>3</sup>, Shintaro Yasui<sup>4</sup>, András Kovács<sup>5</sup>, Hong Jian Zhao<sup>6</sup>, Jorge Íñiguez<sup>6</sup>, and Hiroshi Naganuma<sup>3,7</sup>

<sup>1</sup>Small Scale Systems Integration and Packaging Center, State University of New York at Binghamton, Binghamton, NY 13902, U.S.A.

<sup>2</sup>Department of Physics, State University of New York at Binghamton, Binghamton, NY 13902, U.S.A.

<sup>3</sup>Department of Applied Physics, Graduate School of Engineering, Tohoku University, Sendai 980-8579, Japan

<sup>4</sup>Laboratory for Materials and Structures, Tokyo Institute of Technology, Yokohama 226-8502, Japan

<sup>5</sup>Ernst Ruska-Centre for Microscopy and Spectroscopy with Electrons (ER-C), Peter Grünberg Institute, Forschungszentrum Jülich, Jülich 52425, Germany

<sup>6</sup>Materials Research and Technology Department, Luxembourg Institute of Science and Technology (LIST), L-4422 Belvaux, Luxembourg

<sup>7</sup>Unité Mixte de Physique, CNRS, Thales, Université de Paris-Sud, Université Paris-Saclay, 91767 Palaiseau, France

\*E-mail: itbae@binghamton.edu

Received January 28, 2018; accepted April 19, 2018; published online June 28, 2018

The recent resurgence of bismuth ferrite (BiFeO<sub>3</sub>) as a multiferroic material was triggered by the revelation of its true bulk physical properties in the mid 2000s. Subsequently, multiferroic properties of BiFeO<sub>3</sub> have been found to improve when it is grown as epitaxial film owing to the biaxial strain imposed by substrate materials. Since the crystal and microstructural modifications caused by the strain dominate the multiferroic property changes in BiFeO<sub>3</sub>, tremendous efforts have been devoted to the investigation of structural changes in epitaxial BiFeO<sub>3</sub> films. However, details about strain-induced structural modifications remain elusive owing to the remarkably complex nature of BiFeO<sub>3</sub>. In this review, we discuss the followings: (1) what are the pros and cons between transmission electron microscopy (TEM) and X-ray diffraction (XRD) techniques, (2) a noble methodology of how to apply TEM and XRD to unambiguously identify crystal symmetries in epitaxial BiFeO<sub>3</sub>, and (3) once crystal symmetries are clearly identified, how can the misfit strain be accurately evaluated. © 2018 The Japan Society of Applied Physics

### 1. Introduction

Multiferroic materials simultaneously exhibit coupled ferroic order parameters. This coupling allows, for example, the control of the magnetic properties of a material through changes in its ferroelectric properties. These materials offer significant promise in a variety of smart energy applications including high-efficiency photovoltaic cells with giant open circuit voltages (>10 V), ultra-low power spintronic-based computing and data storage, piezoelectric-based energy harvesting for self-powered sensor nodes, and the use of very low current mechanisms in the switching of magnetic fields. BiFeO<sub>3</sub> (BFO) is one such material that exhibits both ferroelectricity and *G*-type antiferromagnetism above room temperature.<sup>1-3</sup> Its spontaneous polarization value was originally measured at only  $\sim 6 \mu\text{C cm}^{-2}$  along the [111] pseudocubic orientation, which is lower than expected owing to sample leakage.<sup>4</sup> However, the true spontaneous polarization value of  $\sim 60 \mu\text{C cm}^{-2}$  along the [001] pseudocubic orientation ( $\sim 100 \mu\text{C cm}^{-2}$  along the [111] pseudocubic orientation) was found later with the availability of high-quality bulk BFO materials.<sup>5</sup> Meanwhile, with the availability of high-quality single crystal oxide substrates in the early 2000s, BFO has been grown as thin films on a variety of single crystal oxide substrates in an attempt to modify its physical properties by imparting epitaxial strain to the films.<sup>6,7</sup> As a result, the crystal structure of BFO, i.e., rhombohedral with a space group of *R3c* in bulk form, is found to be flexible enough to adapt over  $\sim 6\%$  percent of lattice strain from substrates, which would, otherwise, cause fracture in its bulk form. For example, various BFO phases have been proposed, such as rhombohedral,<sup>8-12</sup> tetragonal-like,<sup>13-17</sup> orthorhombic,<sup>18</sup> monoclinic,<sup>19-22</sup> orthorhombic-like monoclinic,<sup>23</sup> and triclinic,<sup>24</sup> depending on the crystal structures and lattice parameters of the substrates used. In addition, theoretical calculations demonstrate the existence of multiple

metastable BFO phases as a function of strain and temperature.<sup>25</sup> Despite these efforts, the crystal structure within BFO thin films and its associated impact on spontaneous polarization continue to be hotly debated primarily owing to its remarkably complicated nature as pointed out by a recent review article.<sup>26</sup> This implies that the crystallographic details of BFO thin films remain to be clarified.<sup>26</sup>

In most of the previous experimental works dealing with BFO thin films, pseudocubic notation has been used to intuitively describe in-plane and out-of-plane directions of BFO with respect to those of underlying substrates. However, pseudocubic notation cannot accurately describe the rhombohedral nature of the BFO crystal structure because it disregards the  $\sim 0.55^\circ$  rhombohedral distortion in the BFO unit cell as well as rhombohedral shifts in basis atom locations in the unit cell.<sup>27</sup> In order to precisely describe the crystal structure of BFO, either rhombohedral or hexagonal notation should be used. This is particularly important to precisely evaluate the stress/strain effect on epitaxially grown BFO films because their crystal structure and/or lattice parameters are known to be flexible enough to accommodate many percent of misfit strain induced by substrates.<sup>7,28</sup> Another conventional aspect of using pseudocubic notation for BFO is that its pseudocubic lattice parameter of  $\sim 0.396 \text{ nm}$  is simply compared with that of substrate materials to estimate the lattice strains imposed by the substrate materials. This means that BFO growth orientation is assumed to be the same as that of the underlying substrate. For example, the (001) BFO is assumed to grow on the (001) SrTiO<sub>3</sub> substrate. While this might be a reasonable assumption for some substrate materials, the possibility of BFO growing with different orientations with different crystal structures is excluded with this assumption.

In addition, almost all of the X-ray diffraction (XRD) based studies dealing with structural alteration in BFO thin

films have assumed BFO unit cell distortion from its undistorted pseudocubic unit cell to interpret location shift and peak splits found in Bragg's reflections from BFO.<sup>5,13–22</sup> However, it is worth pointing out that the *locations of basis atoms* in the BFO unit cell should change when the unit cell distortion occurs. If the changes in the locations of basis atoms are sufficient to modify the symmetry of the BFO crystal structure, the ramification of which should include generation (and/or removal) of Bragg's reflections in the reciprocal space. This effect can be particularly important for BFO in that BFO, being the combination of three constituent atoms, generates more complicated effects in the reciprocal space than materials with two (or one) constituent atoms do. Thus, in order to understand the crystal structure as well as strain status within BFO thin films, it is imperative to consider both of the *unit cell symmetry*, i.e., lattice parameter, as well as the *locations of basis atoms* in the BFO unit cell by utilizing transmission electron microscopy (TEM) and XRD techniques. While TEM readily provides wide-range reciprocal space information up to  $Q$  (scattering vector)  $\simeq 220 \text{ nm}^{-1}$  including, for instance, crystal symmetry and existence of extra Bragg's reflections to adequately identify the overall BFO crystal structure,<sup>29,30</sup> XRD can provide localized reciprocal space information with exceptional precision that is highly effective for precise *lattice strain* evaluation based on BFO crystal structure identified by TEM.

The objectives of this review are two folds as follows:

(1) In Sect. 3, we describe how TEM and structure factor calculation can be utilized to precisely determine BFO crystal symmetry, i.e., its crystal structure, as well as its epitaxial relationship with underlying substrate materials. While Sect. 3.1 focuses on how the rhombohedral symmetry in BFO can be unambiguously distinguished from other possible symmetries, Sect. 3.2 is about a methodology to determine a new BFO symmetry when none of the previously known BFO crystals match the new BFO symmetry. Thus, Sect. 3 is solely dedicated to the discussion about the precise BFO *symmetry identification*.

(2) In Sect. 4, we discuss how *variations within rhombohedral nature* in BFO can be precisely evaluated by XRD technique once BFO symmetry is confirmed as rhombohedral by TEM, XRD, and structure factor calculation.

## 2. Experimental methods

### 2.1 BFO thin film growth

An ultrahigh-vacuum ( $<2 \times 10^{-6} \text{ Pa}$ ) radio-frequency (rf) magnetron sputtering technique was used with a growth temperature of  $\sim 550 \text{ }^\circ\text{C}$ . The BFO films discussed in the current study are as follows:

Substrate materials	Substrate orientation	BFO thickness (nm)	Reference
SrTiO <sub>3</sub>	(100)	$\sim 30$	10
SrTiO <sub>3</sub>	(100)	$\sim 300$	11
SrTiO <sub>3</sub>	(100)	$\sim 10$	11
SrTiO <sub>3</sub>	(100)	$\sim 3$	31
LaAlO <sub>3</sub>	(100)	$\sim 380$	23
KTaO <sub>3</sub>	(100)	$\sim 60$	12

### 2.2 TEM and XRD analyses

Cross-sectional TEM samples were prepared by either conventional mechanical polishing combined with Ar ion milling or dual-beam focused ion beam technique, FEI Nova 600. Low energy ion milling was followed by using Fischione 1040 Nanomill with 0.5 kV Ar ion to minimize beam-induced damage. TEM analyses were performed using (1) JEOL JEM-2100F equipped with a Gatan Orius 833 CCD camera for bright-field, high-resolution TEM (HRTEM), and transmission electron diffraction, (2) JEOL JEM-ARM200F equipped with probe and image aberration ( $C_s$ )-correctors and Gatan Enfinium spectrometer for HRTEM, high-angle annular dark field (HAADF)-scanning TEM (STEM) imaging and electron energy loss spectroscopy (EELS), (3) a FEI Titan<sup>2</sup> G2 80-200 probe  $C_s$ -corrected TEM equipped with a Gatan Enfinium spectrometer for HAADF-STEM imaging and EELS.

XRD data were obtained using a Bruker D8 discover four-circle X-ray diffractometer using Cu K $\alpha$  radiation. A two-dimensional area detector (Hi-STAR) was used for X-ray reciprocal space mapping (XRSM). XRSM data were compared with those obtained by transmission electron diffraction data.

## 3. Evaluation of biaxial-strain-driven symmetry modification using TEM combined with structure factor calculation

### 3.1 BFO films grown on (100) SrTiO<sub>3</sub> substrate: Sample thickness effect on BFO crystal structure

Figure 1(a) shows a cross-sectional bright-field (BF) TEM image of  $\sim 30 \text{ nm}$  BFO grown on a (100) SrTiO<sub>3</sub> (STO) substrate along the  $[010]_{\text{STO}}$  zone axis. In order to study the crystal structure of BFO, nano-beam electron diffraction (NBED) patterns were obtained from the BFO film and STO substrate with a  $\sim 10 \text{ nm}$  probe as shown in Figs. 1(b) and 1(d). At first glance, the crystal structure of BFO seems to be the same as that of the STO substrate because the four fold symmetry of Bragg's reflections found in BFO [i.e., Fig. 1(b)], is the same as that in STO [i.e., Fig. 1(d)]. While it is tempting to assume that BFO is forced to grow a cubic-perovskite crystal owing to the biaxial strain imposed by the cubic-perovskite STO substrate, it is required to verify whether rhombohedral BFO as well as other BFO phases could possess any zone axis that could show the same four fold symmetry in the NBED pattern. In order to address this issue, the structure factor,  $F_{hkl}$ , where  $hkl$  represents a specific Bragg's reflection, was calculated on the basis of kinematical approximation:

$$F_{hkl} = \sum_n f_n \exp[2\pi i(hx_n + ky_n + lz_n)],$$

where  $f_n$  is the atomic scattering factor for atom  $n$  at fractional coordinates  $(x_n, y_n, z_n)$ . Note that the structure factor can be calculated only for the BFO phases that provide the necessary crystallographic information including the (1) *lattice parameter* and (2) *basis atom locations* in a unit cell. Crystallographic details about nine different BFO phases as well as the STO substrate can be found elsewhere.<sup>10,11,23</sup> Interestingly, it is found that the  $[241]$  zone axis of rhombohedral BFO (r-BFO) matches well that in Fig. 1(b) as shown in Fig. 1(c) in terms of symmetry and locations of Bragg's reflections. This provides another possibility for interpreting Fig. 1(b), i.e., the rhombohedral crystal structure, in addition to the possibility of cubic-perovskite crystal structure for the BFO

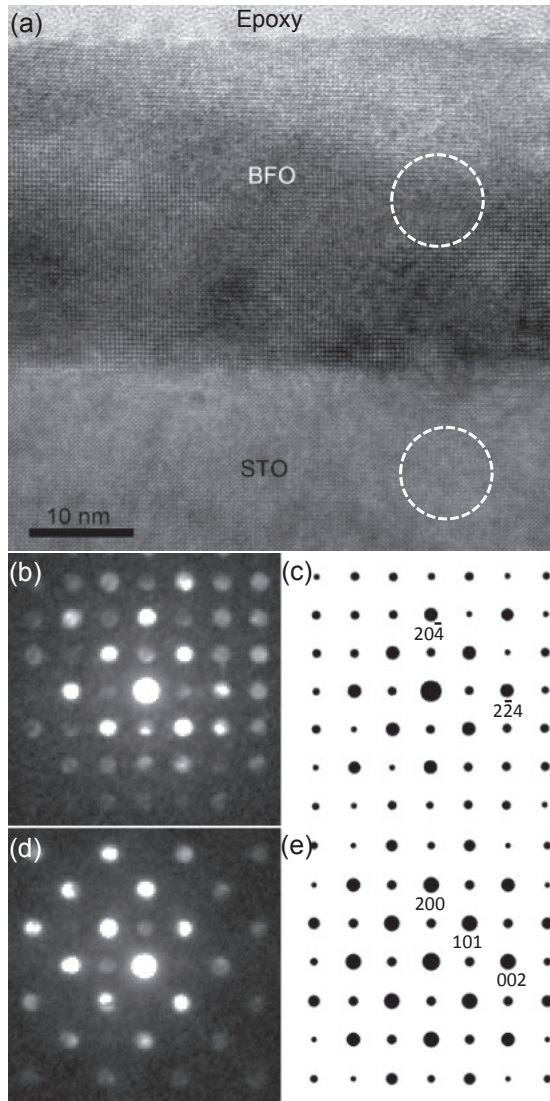


**Fig. 1.** (a) Cross-sectional BF TEM image of ~30-nm-thick BFO film along  $[010]_{\text{STO}}$  zone axis with NBED patterns from the encircled areas of (b) BFO film and (d) STO substrate. The corresponding structure factor calculations are shown in (c) and (e), respectively. Reproduced from Ref. 10 with permission.

film. The structure factor was also calculated for the  $[010]$  zone axis of the STO substrate to investigate the epitaxial relationship between the BFO film and the STO substrate as shown in Fig. 1(e). In order to determine to which crystal structure the BFO film corresponds, another cross-sectional TEM sample was prepared along the  $[011]_{\text{STO}}$  zone axis as shown in Fig. 2(a). NBED patterns from BFO and STO were obtained from the encircled areas in Fig. 2(a) and are shown in Figs. 2(b) and 2(d). Unlike the cross-section along the  $[010]_{\text{STO}}$  orientation, the geometry of Bragg's reflections in Fig. 2(b), i.e., the BFO film, is distinctively different from that in Fig. 2(d), i.e., the STO substrate, owing to extra Bragg's reflections such as  $[11\bar{3}]$  and  $[2\bar{1}\bar{3}]$  showing up only in Fig. 2(b), which are not found in Fig. 2(d). Note that some reflections denoted by arrows result from double diffraction.<sup>10,11</sup> This indicates that the crystal structure in the BFO overlayer is different from that in the STO substrate, i.e., cubic-perovskite. In fact, the structure factor calculation clearly revealed that the NBED pattern in Fig. 2(b) can be interpreted only by the  $[211]$  zone axis of r-BFO, as shown in

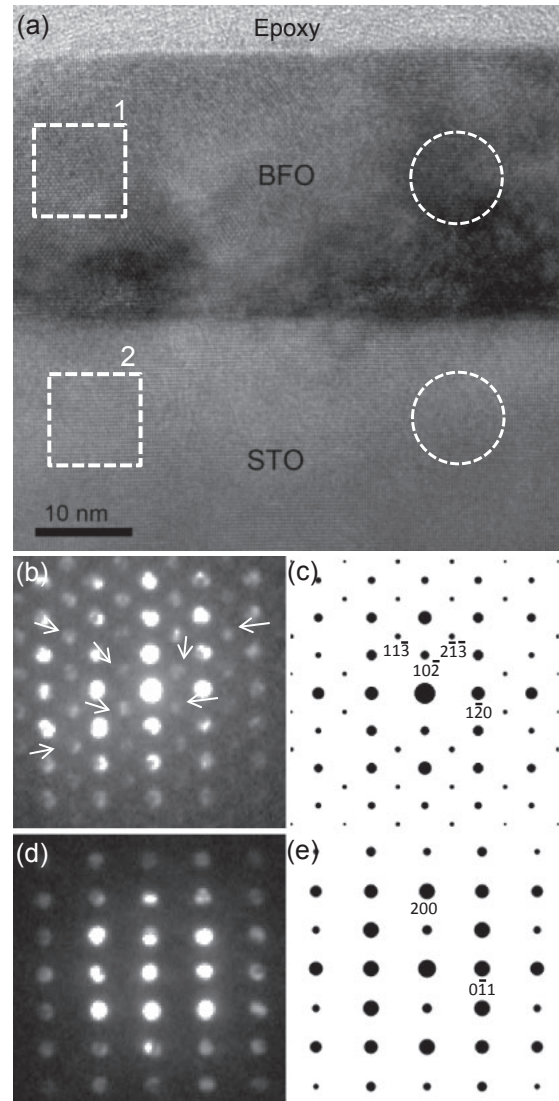


**Fig. 2.** (a) Cross-sectional BF TEM image of ~30-nm-thick BFO layer along  $[011]_{\text{STO}}$  zone axis with NBED patterns from the encircled areas of (b) BFO film and (d) STO substrate. The corresponding SF calculations are shown in (c) and (e), respectively. Reproduced from Ref. 10 with permission.

Fig. 2(c). In addition, structure factor calculation also proved that cubic-perovskite *cannot* reproduce the NBED pattern in Fig. 2(b). The structure factor along  $[011]_{\text{STO}}$  was calculated to investigate its epitaxial relationship with the r-BFO film as shown in Fig. 2(e). In order to demonstrate that the difference in the geometry of Bragg's reflections found between Figs. 2(b) and 2(d) is not associated with CCD camera artifact, HRTEM images of the BFO film and the STO substrate were acquired from the areas enclosed in squares denoted as 1 and 2 in Fig. 2(a), and shown in Figs. 3(a) and 3(b), respectively. Although differences in crystal structures between Figs. 3(a) and 3(b) are difficult to identify from the HRTEM image contrasts, their fast Fourier transform (FFT) patterns are clearly different by revealing the same characteristics found in the NBED patterns, i.e., the extra Bragg's reflections found only in the BFO film. Thus, it is concluded that the extra Bragg's reflections found in Fig. 2(b) are not from CCD camera artifact but from the crystal structure of r-BFO. It is worth noting that the angle between the  $[241]$  [= Fig. 1(b)] and the  $[211]$  [= Fig. 2(b)] r-BFO is calculated

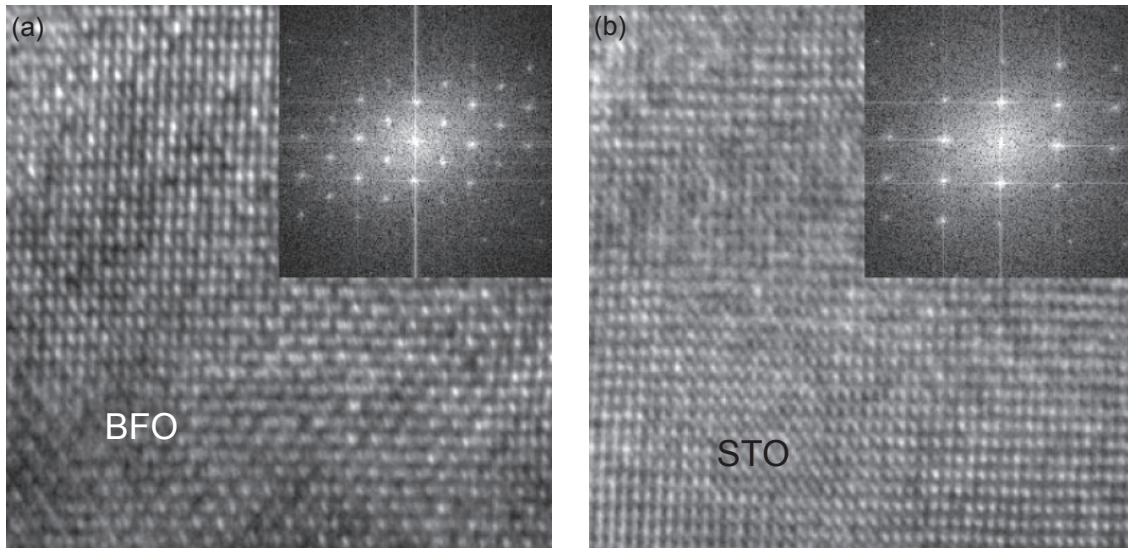


**Fig. 3.** HRTEM images of (a) the squared BFO and (b) STO areas in Fig. 2(a). FFT patterns for the areas are shown in the insets. Reproduced from Ref. 10 with permission.

to be  $\sim 45.0^\circ$  which is in excellent agreement with the angle between the [010] [= Fig. 1(d)] and the [011] [= Fig. 2(d)] STO orientations, which is  $45.0^\circ$ . This also verifies the validity of the current NBED and structure factor calculation results. Thus, the epitaxial relationship between BFO and STO is as follows:

$$\begin{aligned}
 & [241] \text{ of r-BFO} \parallel [010] \text{ of STO}; \\
 & (10\bar{2}) \text{ of r-BFO} \parallel (100) \text{ of STO [see Figs. 1(c) and 1(e)],} \\
 & [211] \text{ of r-BFO} \parallel [011] \text{ of STO}; \\
 & (10\bar{2}) \text{ of r-BFO} \parallel (100) \text{ of STO [see Figs. 2(c) and 2(e)].}
 \end{aligned}
 \tag{1}$$

In order to further verify the current analytical methodology, two new NBED patterns from r-BFO and STO were obtained by tilting the  $[010]_{\text{STO}}$  sample by  $\sim 25^\circ$  inside the TEM column as shown in Figs. 4(a) and 4(c), respectively. Note that the symmetry of Bragg's reflections in Fig. 4(a) is identical to that in Fig. 4(c), which seems to imply that the crystal structure of the r-BFO film is the same as that of STO. However, structure factor calculation clearly revealed that although Fig. 4(a) corresponds to the  $[441]$  zone axis of r-BFO, Fig. 4(c) corresponds to the  $[13\bar{1}]$  zone axis of cubic-perovskite STO, as revealed by structure factor calculation shown in Figs. 4(b) and 4(d), respectively. The angle between  $[13\bar{1}]$  and  $[010]$  of STO is calculated to be  $\sim 25.2^\circ$ , which is in excellent agreement with  $\sim$ the angle of  $25^\circ$  between the  $[441]$  and  $[241]$  of r-BFO. This further confirms validity of the current approach for BFO phase identification.

The painstaking efforts of structure factor calculations followed by careful comparisons for all the reported crystal symmetries for BFO including the pseudocubic symmetry lead us to an invaluable insight as follows. Given that the only difference between pseudocubic and rhombohedral symmetries is the rhombohedral distortion, i.e., the  $\alpha$  angle of  $\sim 0.55^\circ$  followed by the rhombohedral shifts in basis atom locations, the extra Bragg's reflections showing up only in rhombohedral BFO, i.e., their disappearance in all other BFO symmetries including the pseudocubic, can be considered as a signature characteristic of the rhombohedral nature in

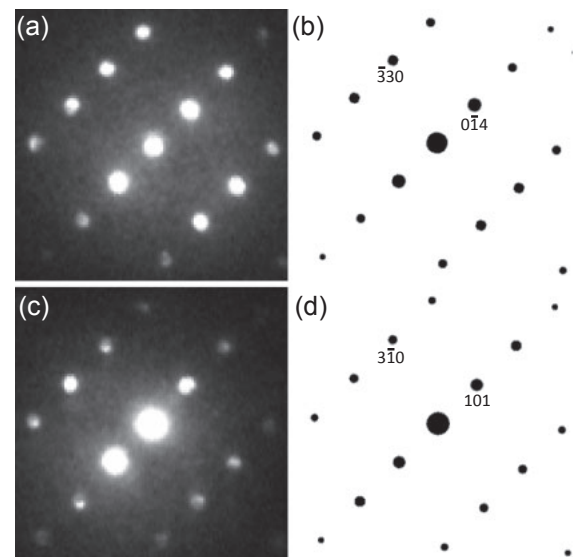


**Fig. 4.** NBED patterns from BFO (a) film and STO substrate (b) from Fig. 1(a) with  $\sim 25^\circ$  in situ tilt. The corresponding structure factor calculation results are shown in (b) and (d). Reproduced from Ref. 10 with permission.

BFO crystals. In other words, the disappearance of the extra Bragg's reflections in BFO diffraction pattern confirms the rhombohedral symmetry breakdown in terms of *lattice parameters* as well as *basis atom locations* in BFO crystals. It is also worth noting that the literature shows slight structural variations in bulk rhombohedral BFO. For example, while the  $a$  and  $c$  lattice parameters in hexagonal notation reported in Ref. 27 are 0.57874 and 1.38688 nm, those in Ref. 35 are 0.561853 and 1.39824 nm, respectively. This leads to the fact that the  $a$  and  $c$  lattice parameters in bulk BFO have variations of  $\sim 0.82$  for  $a$  and  $\sim 0.71\%$  for  $c$  together with slight variations in the locations of basis atoms. These variations in  $a$  and  $c$  lattice parameters, and basis atom locations convert to the variations in lattice parameters  $a$  and  $\alpha$  angles in rhombohedral notation. Because of these variations, i.e., slight flexibility in the rhombohedral nature in BFO crystals, slight location shifts found in a couple (or a

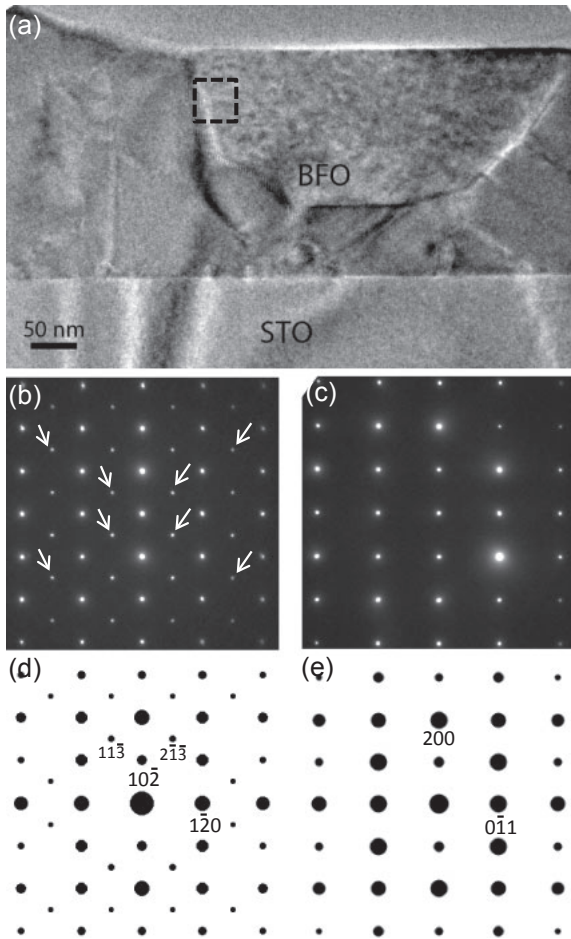


**Fig. 5.** Cross-sectional BF TEM image of ~300 nm BFO film along  $[011]_{\text{STO}}$  zone axis with selected-area electron diffraction patterns from (b) BFO film and (c) STO substrate. Structure factor calculations for BFO and STO are shown in (d) and (e). Some reflections indicated by white arrows in (b) result from double diffraction. Reproduced from Ref. 11 with permission.

few) of pseudocubic Bragg's reflections in electron diffraction or XRD are not sufficient to prove the breakdown of the rhombohedral symmetry in BFO crystals. In other words, rhombohedral symmetry breakdown in BFO crystals should be determined by the disappearance of the extra Bragg's reflections rather than by slight location shifts in out-of-plane and/or in-plane Bragg's reflections that are defined by the pseudocubic notation.

Thus, ~300 nm BFO film was prepared along the  $[011]_{\text{STO}}$  zone axis (which is the zone axis that can confirm either the existence or disappearance of extra Bragg's reflections) to investigate the effect of BFO film thickness on the BFO crystal symmetry, and its cross-sectional image is shown in Fig. 5(a). Selected-area electron diffraction patterns from BFO and STO are shown in Figs. 5(b) and 5(c) with their corresponding structure factor calculation results [see Figs. 5(d) and 5(e), respectively]. Note that the Bragg's reflections indicated by white arrows in Fig. 5(b) are attributed to double diffraction as mentioned earlier. One can immediately notice that the rhombohedral characteristic of BFO in Fig. 5(d) stands out with the signature Bragg's reflections such as  $(11\bar{3})$  and  $(2\bar{1}\bar{3})$ . In order to further verify the rhombohedral nature in BFO, a HRTEM images was obtained using JEOL JEM-ARM200F and shown in Fig. 6(a) with the corresponding HRTEM image simulation result using the multislice method [see Fig. 6(b)].

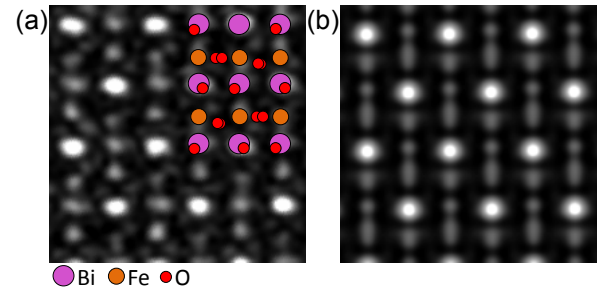


**Fig. 6.** (Color online) (a) HRTEM image from the squared BFO area in Fig. 5(a), and (b) shows the corresponding image simulation using multislice method. The simulated image based on rhombohedral BFO phase well interprets the characteristics of the HRTEM image. Reproduced from Ref. 11 with permission.

The simulation parameters used for Fig. 6(b) are  $E = 300$  keV,  $C_s = 1$   $\mu\text{m}$ , defocus = 9 nm, and BFO thickness = 40 nm. One can readily recognize that the locations of Bi atom columns show alternating "strong" and "weak" contrasts horizontally as well as vertically in Fig. 6(b). This characteristic is well reproduced in Fig. 6(b), which verifies that the crystal structure of BFO is rhombohedral.<sup>11)</sup>

Figures 7(a) and 8(a) show cross-sectional BF TEM images of ~10- and ~3-nm-thick BFO films along the  $[011]_{\text{STO}}$  zone axis, respectively, to further investigate the thickness effect on thinner BFO films. While the NBED patterns in Figs. 7(c) and 8(c) show the cubic-perovskite characteristic of the  $[011]_{\text{STO}}$  zone axis, those for ~10- and ~3-nm-thick BFO films [see Figs. 7(b) and 8(b)] show the rhombohedral characteristic, i.e., the extra Bragg's reflections discussed earlier. These results clearly reveal that the BFO films grown on (100) STO substrate possess the rhombohedral crystal symmetry when their thicknesses are between from ~3 to ~300 nm. However, the possibility of slight differences, i.e., variations, within the rhombohedral symmetry in each BFO film could not be excluded, and needs further study using, for example, the XRD technique that provides better accuracy than the electron diffraction technique in terms of measuring the locations of Bragg's reflections.

Now, let us consider why r-BFO films grow with the epitaxial relationship with the STO substrate denoted as (1). Figure 9 show atomistic models at the BFO/STO interface along the (a)  $[010]_{\text{STO}}$  ( $= [241]_{\text{r-BFO}}$ ) and (b)  $[011]_{\text{STO}}$  ( $= [211]_{\text{r-BFO}}$ ) zone axes. Note that these models are constructed by undistorted r-BFO and STO materials. It can be readily noticed that the lattice plane spacings between r-BFO and STO along the in-plane direction are highly similar. For example, the differences in the in-plane lattice spacings are ~2.3% in Fig. 9(a) and ~1.8% in Fig. 9(b), indicating that the lattice mismatch at BFO/STO is minimal. Thus, the minimal lattice mismatch at BFO/STO interface is believed to be the reason for the epitaxial relationship denoted as (1).

### 3.2 BFO film grown on (100) $\text{LaAlO}_3$ substrate: Highly compressive biaxial strain effect

Figure 10(a) shows a cross-sectional BF TEM image of BFO grown on  $\text{LaAlO}_3$  (LAO) along the  $[241]_{\text{LAO}}$  zone axis. One can readily notice that the ~380-nm-thick BFO film consists of two zones with darker (denoted as zone I) and brighter (denoted as zone II) contrasts. In order to acquire information about the crystal structure in each zone. The NBED patterns were obtained with ~80 nm probe size from zones II and I as

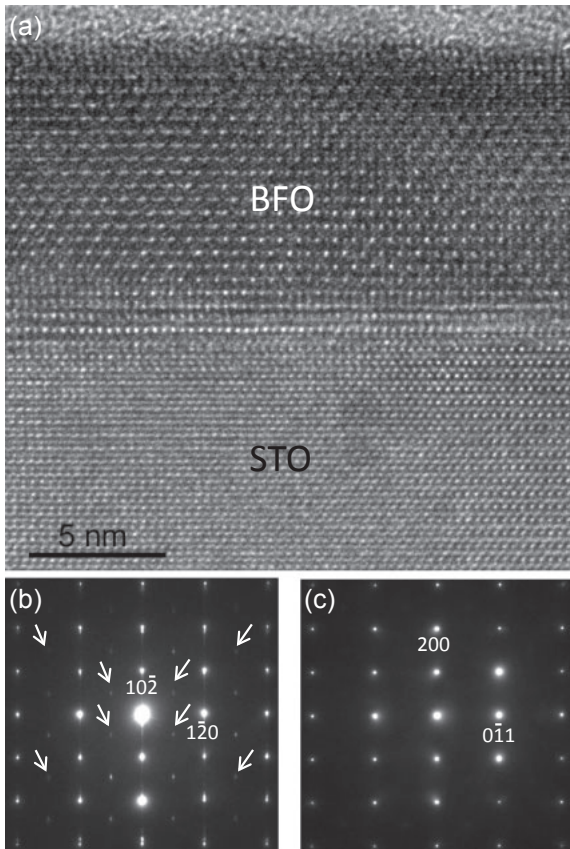


**Fig. 7.** (a) Cross-sectional BF TEM image of  $\sim 10$  nm BFO film along  $[011]_{\text{STO}}$  zone axis with NBED patterns from (b) BFO film and (c) STO substrate. Some reflections indicated by white arrows in (b) result from double diffraction. Reproduced from Ref. 11 with permission.

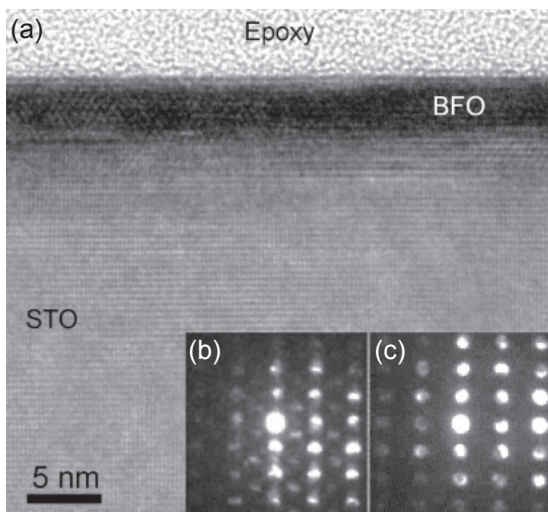


**Fig. 8.** (a) Cross sectional BF TEM image of  $\sim 3$  nm BFO film along  $[011]_{\text{STO}}$  zone axis with NBED patterns from (b) BFO film and (c) STO substrate.

shown in Figs. 10(b) and 10(c). NBED pattern from LAO [see Fig. 10(d)] was obtained also to investigate the epitaxial relationship between BFO and LAO. One can readily find that the symmetry in Fig. 10(b) is the same as that in Fig. 10(d), indicating that the crystal structure of BFO within zone II is rhombohedral. The corresponding structure factor calculation results shown in Fig. 10(e) clearly reveal that the crystal structure is rhombohedral with the space group  $R3c$ . On the

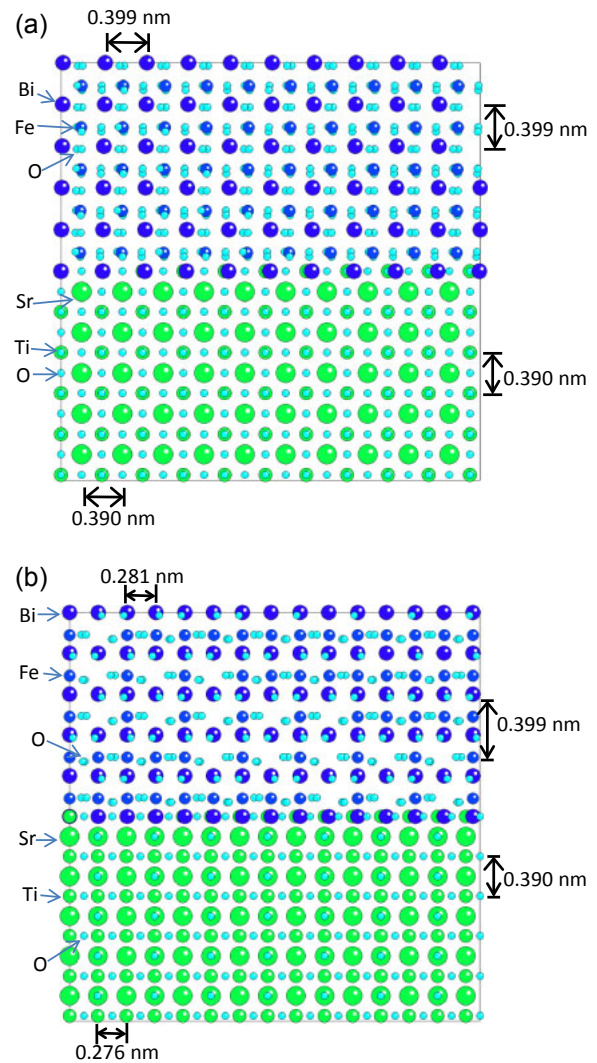


**Fig. 9.** (Color online) Atomistic models based on epitaxial relationships, demonstrating BFO/STO interface along (a)  $[010]_{\text{STO}}$  ( $= [241]_{\text{r-BFO}}$ ) and (b)  $[011]_{\text{STO}}$  ( $= [211]_{\text{r-BFO}}$ ) zone axes. Note that the misfit strains at BFO/STO (when viewed from each zone axis) are calculated to be 2.3 and  $\sim 1.8\%$ , respectively. Reproduced from Ref. 10 with permission.

other hand, the symmetry and locations of Bragg's reflections in Fig. 10(c) are clearly different from those in Fig. 10(b). This indicates crystal structure of BFO within zone I is not rhombohedral. Since none of the BFO phases reported previously can reproduce the NBED pattern in Fig. 10(c), first-principles calculation based on the density function theory was implemented using the VASP code.<sup>23)</sup> As a result, the  $[001]$  zone axis from a new monoclinic BFO (m-BFO) crystal, i.e., space group:  $Cm$ ,  $a = 0.9262$  nm,  $b = 0.7582$  nm,  $c = 0.3791$  nm,  $\alpha = \gamma = 90^\circ$ ,  $\beta \approx 90^\circ$  (see Table I in Ref. 23 for locations of basis atoms in the unit cell), was found to accurately reproduce the NBED pattern of Fig. 10(c) as revealed in Fig. 10(f).<sup>23)</sup> In order to further confirm the validity of the m-BFO structure, a cross-sectional sample of another zone axis, i.e.,  $[211]_{\text{LAO}}$ , is prepared, and its BF TEM image is shown in Fig. 11(a). NBED patterns from BFO zone II, BFO zone I, and LAO are shown in Figs. 11(b)–11(d), respectively. Note that the intensity maxima denoted by white arrows in Figs. 11(b) and 11(d) are attributed to double diffractions.<sup>23)</sup> The symmetry of Bragg's reflections in Fig. 11(b) is readily recognizable to be the same as that in

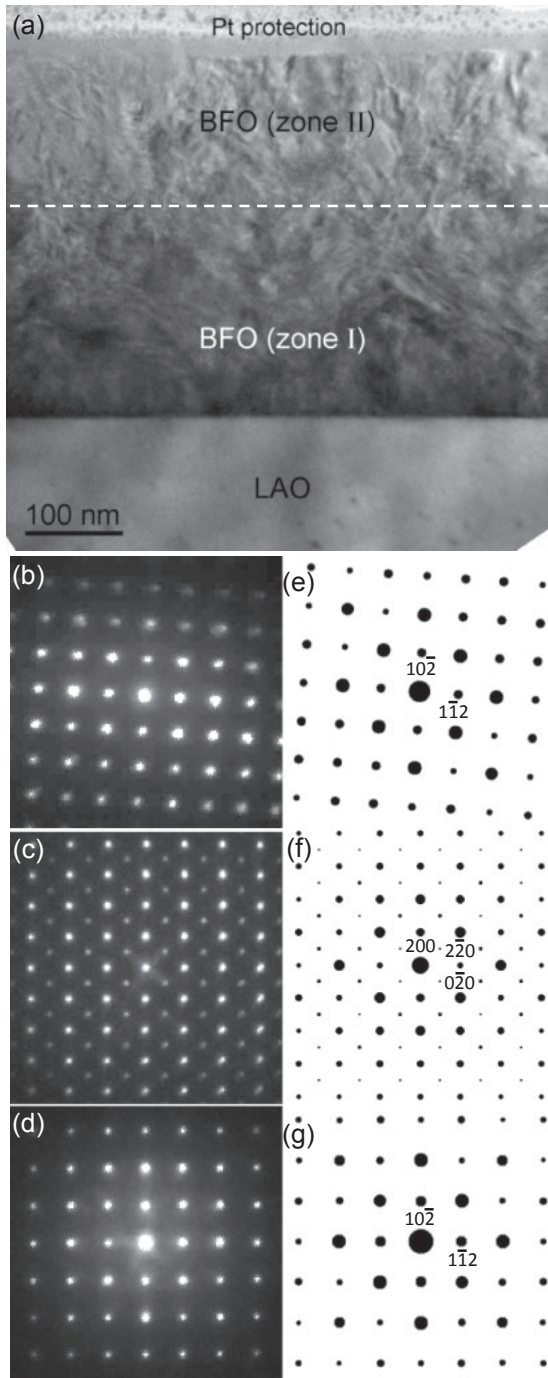


**Fig. 10.** (a) Cross-sectional BF TEM image of ~380 nm BFO film on LAO substrate along  $[241]_{\text{LAO}}$  zone axis with NBED patterns from (b) zone II, (c) zone I, and (d) LAO substrate. Structure factor calculation for the corresponding NBED patterns are shown in (e), (f), and (g), respectively. Reproduced from Ref. 23 with permission.

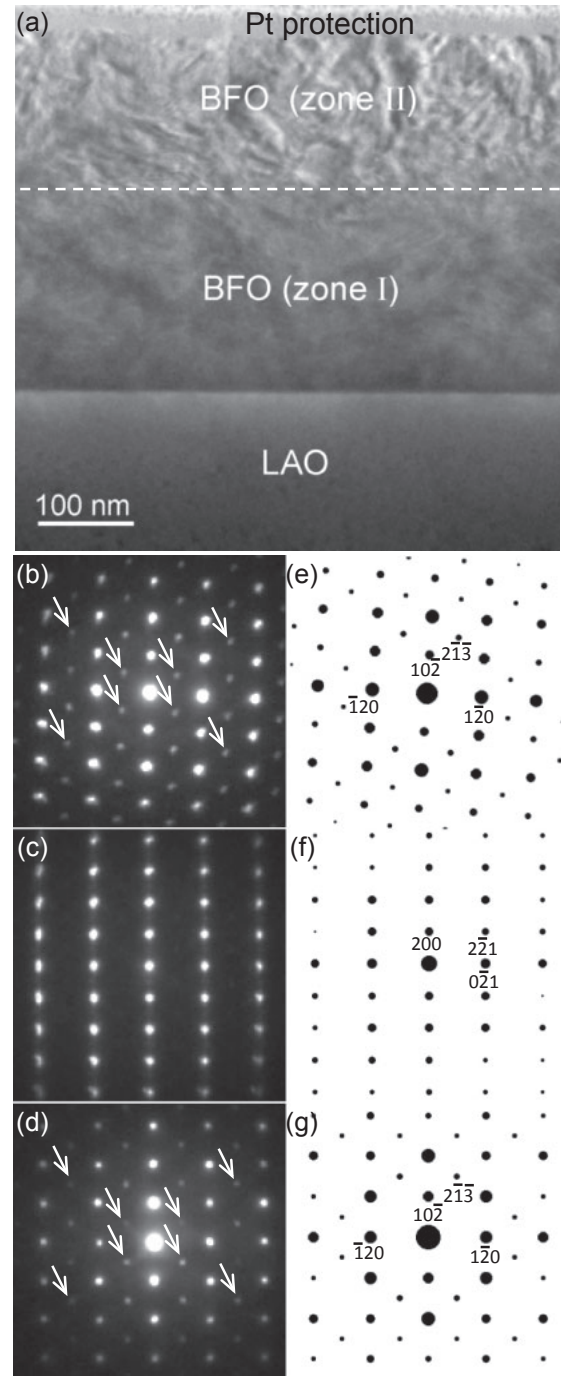


**Fig. 11.** (a) Cross-sectional BF TEM image of ~380 nm BFO film on LAO substrate along  $[211]_{\text{LAO}}$  zone axis with NBED patterns from (b) zone II, (c) zone I, and (d) LAO substrate. Structure factor calculation for the corresponding NBED patterns are shown in (e), (f), and (g), respectively. Reproduced from Ref. 23 with permission.

Fig. 11(d), suggesting that BFO within zone II has the rhombohedral structure. Note that the signature reflections such as  $(11\bar{3})$  and  $(2\bar{1}\bar{3})$  are clearly visible in Figs. 11(b) and 11(d), verifying their rhombohedral nature in the crystal symmetries. However, the symmetry and locations of Bragg's reflections in Fig. 11(c) are different from those in Figs. 11(b) and 11(d) with no such signature reflections, indicating that the BFO crystal structure within zone I is not the rhombohedral structure. Structure factor calculation results for Figs. 11(b)–11(d) are shown in Figs. 11(e)–11(g), respectively. They indeed reveal that BFO within zones II and I

corresponds to the  $[211]$  zone axis of rhombohedral BFO, i.e., r-BFO, [see Fig. 11(e)] and  $[012]$  monoclinic BFO, i.e., m-BFO, [see Fig. 11(f)], respectively. On the basis of the NBED analysis results in Figs. 10 and 11, the epitaxial relationship between zone I, i.e., m-BFO, and the LAO substrate is as follows:

$$\begin{aligned}
 [001]_{\text{m-BFO}} &\parallel [241]_{\text{LAO}}; \\
 (200)_{\text{m-BFO}} &\parallel (10\bar{2})_{\text{LAO}} \text{ (along } [241]_{\text{LAO}}), \\
 [012]_{\text{m-BFO}} &\parallel [211]_{\text{LAO}}; \\
 (200)_{\text{m-BFO}} &\parallel (10\bar{2})_{\text{LAO}} \text{ (along } [211]_{\text{LAO}}). \quad (2)
 \end{aligned}$$

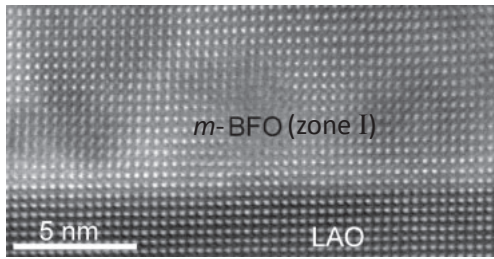


**Fig. 12.**  $[241]_{\text{LAO}}$  cross-sectional HAADF-STEM image at m-BFO (= zone I)/LAO interface showing smooth lattice plane transition from LAO to m-BFO with no obvious sign of lattice imperfections. Reproduced from Ref. 23 with permission.

This result confirms the validity of the monoclinic structure calculated using density function theory. To further study the growth mechanism of zones I and II on LAO, an atomic resolution high-angle annular dark-field (HAADF)-scanning TEM (STEM) image was obtained at m-BFO/LAO interface and shown in Fig. 12. Note that the lattice plane in LAO runs smoothly through m-BFO with no apparent sign of lattice imperfections such as misfit dislocations. This indicates that (1) the LAO/m-BFO interface is atomistically coherent and (2) the biaxial misfit strain imposed on the m-BFO layer may not be released. If atomistic models are constructed on the basis of the epitaxial relationship (2) as shown in Fig. 13, one can readily notice the lattice misfits between m-BFO/LAO viewed along  $[241]_{\text{LAO}}$  [see Fig. 13(a)] and  $[211]_{\text{LAO}}$  [see Fig. 13(b)] are  $\sim 0.0\%$ . On the other hand, the lattice mismatch between r-BFO and LAO along the in-plane direction is, for example,  $\sim 5.3\%$  when calculated for  $(1\bar{1}2)$  of r-BFO and  $(1\bar{1}2)$  of LAO. Thus, it is believed that the minimal lattice mismatch of  $\sim 0.0\%$  found between m-BFO and the LAO substrate is the reason why m-BFO rather than r-BFO grows on the LAO substrate. However, as m-BFO grows further, the biaxial constraint originating from LAO should weaken such that m-BFO can no longer maintain its monoclinic structure. This will lead to r-BFO growth, i.e., its equilibrium BFO phase, on top of m-BFO.

Note that BFO has been reported to epitaxially grow on the LAO substrate as the so-called “supertetragonal” or “pseudotetragonal” phase with a  $c/a$  ratio of  $\sim 1.24$ .<sup>15,17,32–34</sup> Hereafter, we call this as t-BFO. Zeches et al. have obtained the unit cell size of t-BFO with  $a \simeq 0.384$  nm,  $b \simeq 0.376$  nm, and  $c \simeq 0.465$  nm by measuring in-plane and out-of-plane Bragg’s reflections by XRSM and  $\theta$ - $2\theta$  XRD analysis.<sup>15</sup> They performed atomic resolution STEM imaging of t-BFO to demonstrate the structural difference between t-BFO and r-BFO.<sup>15</sup> Interestingly, electron diffraction and FFT patterns from t-BFO (provided in supporting material) clearly show characteristics that are highly comparable to those in Fig. 10(c), i.e., NBED along the  $[001]_{\text{m-BFO}}$  zone axis, in terms of the symmetry and intensity profile of Bragg’s reflections.<sup>15</sup> Infante et al. also reported on t-BFO grown on LAO with its unit cell being  $a \simeq 0.379$  nm (in-plane orientation) and  $c \simeq 0.466$  nm (out-of-plane orientation) using the HRTEM technique combined with geometric phase analysis.<sup>32</sup> More recently, Rossell et al.<sup>33</sup> and Pailloux et al.<sup>34</sup> have also reported that the  $c/a$  ratios of t-BFO were  $\sim 1.27$  and  $\sim 1.24$ , respectively. It is interesting to note that the out-of-plane lattice spacing/in-plane lattice spacing along

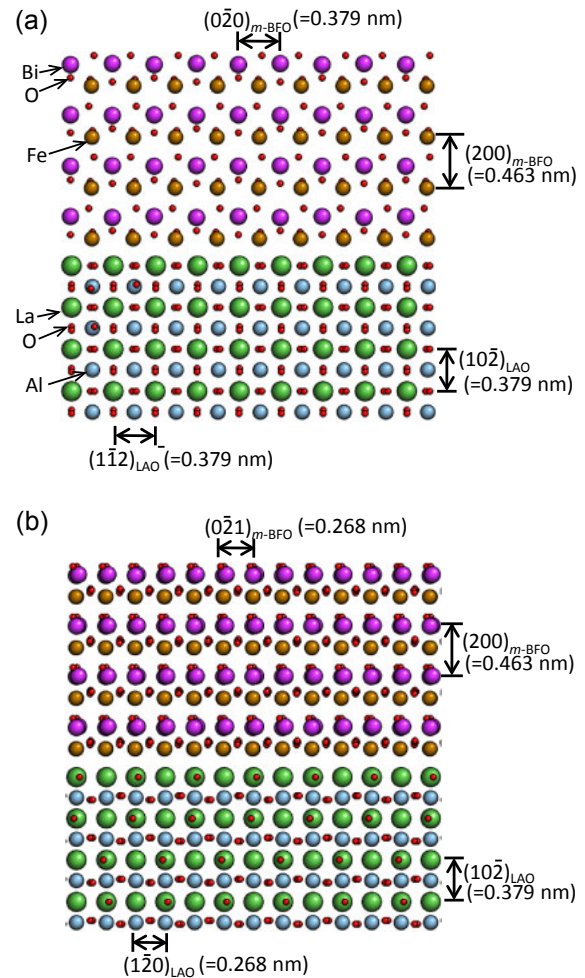


**Fig. 13.** (Color online) Atomistic models at m-BFO (= zone I)/LAO interface along (a)  $[241]_{\text{LAO}}$  ( $= [001]_{\text{m-BFO}}$ ) and (b)  $[211]_{\text{LAO}}$  ( $[012]_{\text{m-BFO}}$ ) zone axes. Note that the misfit strains at m-BFO/LAO (when viewed from each zone axes) are calculated to be  $\sim 0.0$  and  $\sim 0.0\%$ , respectively. Reproduced from Ref. 23 with permission.

$[241]_{\text{LAO}}$  zone axis for m-BFO is  $\sim 1.22$ . This is highly comparable to the  $c/a$  ratio of  $\sim 1.24$  reported for t-BFO. In particular, Pailloux et al.<sup>34</sup> also prepared a cross sectional TEM sample along the  $[001]_{\text{pseudocubic}}$  LAO substrate for selected-area electron diffraction analysis. The selected-area electron diffraction pattern shows characteristic Bragg’s reflections at the  $1/2(100)_{\text{pseudocubic}}$  BFO. These characteristic Bragg’s reflections together with their symmetry make the pattern highly comparable to those shown in Fig. 10(c). Furthermore, the pyramidal bonding geometry between Fe and O atoms for t-BFO is found to be the same as that found for m-BFO (see Fig. 14). The results shown above seem to indicate that t-BFO is highly comparable to (or possibly the same as) m-BFO discussed here. However, it should be noted that although the morphology of t-BFO in previous works shows slanted and/or vertical grains that grow together with r-BFO along the surface normal direction,<sup>15,17,32–34</sup> m-BFO discussed here shows a lateral thin layer between r-BFO and the LAO substrate. Besides, although the growth technique used for t-BFO are either pulsed laser deposition or molecular beam epitaxy, m-BFO is grown by ultrahigh vacuum rf magnetron sputtering which may provide different BFO film growth kinetics. More importantly, previous works estimate only the size and symmetry of the t-BFO unit cell in terms of

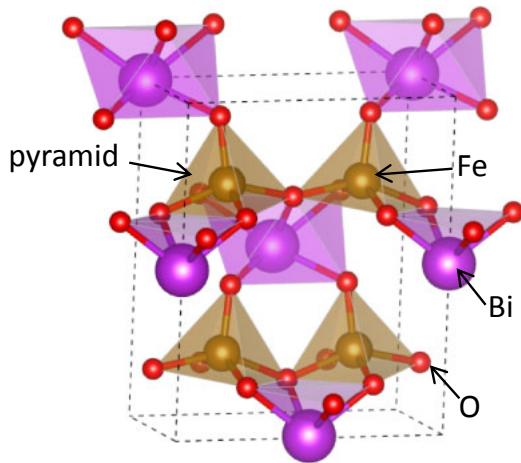


**Fig. 14.** (Color online) Atomic model of m-BFO showing pyramidal bonding geometries between Fe and O. Reproduced from Ref. 23 with permission.

how a t-BFO unit cell is strained (or modified) with respect to r-BFO. Since no complete crystallographic data (specifically the *locations of basis atoms* in a unit cell) for t-BFO are as of yet available, it is not possible to directly compare the structural details of m-BFO (see Table I in Ref. 23) with those of t-BFO. Thus, it is not clear whether m-BFO discussed here is the same as t-BFO or not. Further study is necessary to elucidate this point.

#### 4. Precise strain measurement combining TEM and XRD techniques

Figure 15(a) shows a cross-sectional BF TEM image of ~60 nm BFO grown on the (100)  $\text{KTaO}_3$  (KTO) substrate along the  $[011]_{\text{KTO}}$  zone axis. Note that the BFO films show strain contrasts running across the entire BFO thickness as denoted by white arrows. This indicates biaxial lattice strain imposed by the KTO substrate is not relaxed. An NBED pattern obtained from the BFO layer with ~40 nm probe size is shown in Fig. 15(b). One can readily notice that it corresponds to  $[211]$  of the r-BFO because of r-BFO signature Bragg's reflections such as  $[11\bar{3}]$  and  $[2\bar{1}\bar{3}]$ . None of these reflections appear in the NBED pattern [see Fig. 15(c)] from the KTO substrate that has the cubic-perovskite structure. In order to further study the crystal structure within the BFO film, another BF TEM image of the same sample along the  $[001]$  zone axis is shown in Fig. 16(a). Strain contrasts within the BFO film are still visible, as indicated by white arrows, which is consistent with Fig. 15(a). NBED patterns from the BFO film and KTO substrate are shown in Figs. 16(b) and 16(c). Although the four fold symmetry of Bragg's reflections in Fig. 16(b) is the same as that in Fig. 16(c), Fig. 16(b) is associated *not* with the  $[010]_{\text{pseudocubic BFO}}$  zone axis, but with the  $[241]_{\text{r-BFO}}$  zone axis as discussed earlier. Thus, Figs. 15 and 16 clearly reveal that the crystal structure of the BFO film is indeed *rhombohedral*. On the basis of the results of NBED analysis, the epitaxial relationship is found to be as follows:

- $[211]$  of r-BFO  $\parallel$   $[011]$  of KTO;
- $(10\bar{2})$  of r-BFO  $\parallel$   $(100)$  of KTO,
- $[241]$  of r-BFO  $\parallel$   $[010]$  of KTO;
- $(10\bar{2})$  of r-BFO  $\parallel$   $(100)$  of KTO.

(3)

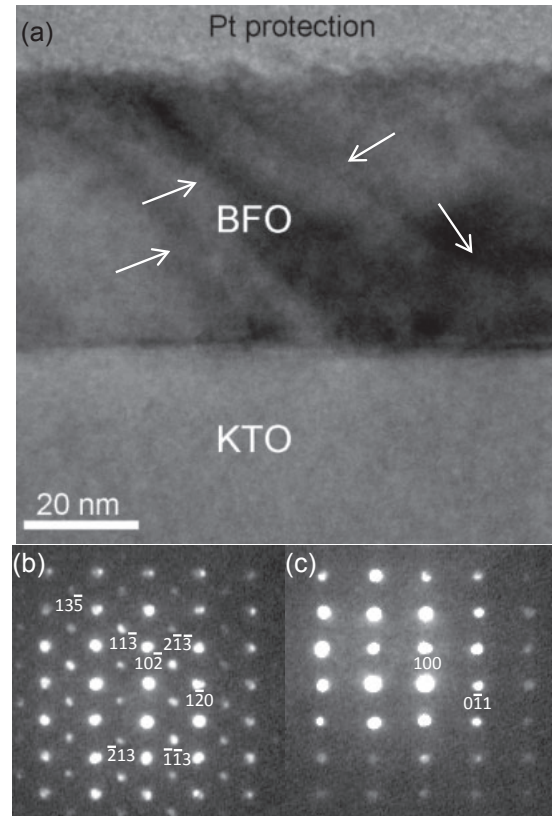


**Fig. 15.** Cross-sectional BF TEM image of ~30 nm BFO grown on KTO substrate along  $[011]_{\text{KTO}}$  zone axis with NBED patterns from (b) BFO film and (c) KTO substrate. Reproduced from Ref. 12 with permission.

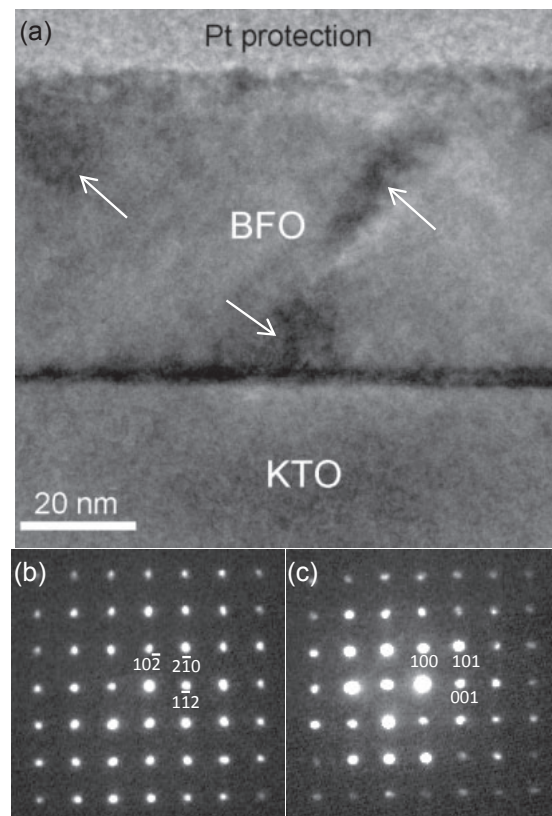


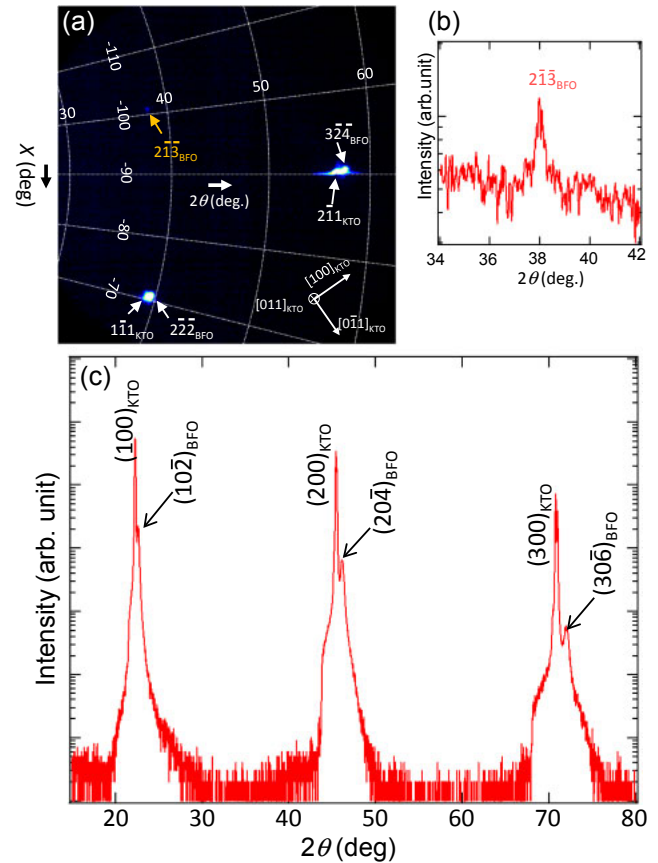
**Fig. 16.** Cross-sectional BF TEM image of ~30 nm BFO grown on KTO substrate along  $[010]_{\text{KTO}}$  zone axis with NBED patterns from (b) BFO film and (c) KTO substrate. Reproduced from Ref. 12 with permission.

Note that the epitaxial relationship (3) found for the KTO substrate is the same as the epitaxial relationship (1) derived for the STO substrate. Atomistic models based on epitaxial relationship (3) reveal that the lattice mismatch at the BFO/KTO interface can be accurately calculated to be  $\sim 0.35\%$ .<sup>12)</sup> This is smaller than  $\sim 0.76\%$  estimated on the basis of the pseudocubic assumption to describe r-BFO. This result suggests that investigation of the epitaxial relationship between the BFO film and the substrate material is required to accurately calculate the true misfit strain applied to BFO. Note that if the BFO film is found to be r-BFO, *hexagonal notation*, rather than pseudocubic notation, is required to accurately describe r-BFO. On the basis of the epitaxial relationships (1) and (3), it is concluded that the BFO film epitaxially grows as r-BFO, i.e., its equilibrium phase, when the misfit strain against the substrate falls between  $\sim 2.3\%$  of compressive strain and  $\sim 0.35\%$  of tensile strain.

It is worth mentioning that despite the importance of the rhombohedral signature Bragg's reflections, i.e., the extra Bragg's reflections, no discussion was made about it until very recently.<sup>10–12,23)</sup> This is presumably because almost all of the previous XRD and TEM works have used pseudocubic notation rather than hexagonal notation to describe the r-BFO crystal. Since pseudocubic notation disregards the  $\sim 0.55^\circ$  rhombohedral distortion as well as the slight shifts in basis atom locations in the unit cell that accordingly follow as a result of the rhombohedral distortion,<sup>27)</sup> the existence of rhombohedral signature Bragg's reflections could well be overlooked, so that no efforts have been made to study those Bragg's reflections.<sup>12)</sup> Figure 17(a) shows a XRSM result near a rhombohedral signature Bragg's reflection, i.e.,  $(2\bar{1}\bar{3})_{\text{r-BFO}}$ , obtained using a two-dimensional area detector as shown in Fig. 17(a). Its intensity is much lower than other fundamental Bragg's reflections such as  $(2\bar{2}\bar{2})_{\text{BFO}}$  and  $(3\bar{2}\bar{4})_{\text{BFO}}$ , as expected from the structure factor calculation in Fig. 2(c) and X-ray powder diffraction result.<sup>35)</sup> However, its signal clearly shows up above the background noise, as revealed in one-dimensional intensity profile along the  $2\theta$  orientation, as revealed in Fig. 17(b). This confirms the consistency among XRD, NBED, and structure factor calculation results in terms of demonstrating the existence of the rhombohedral signature Bragg's reflections.

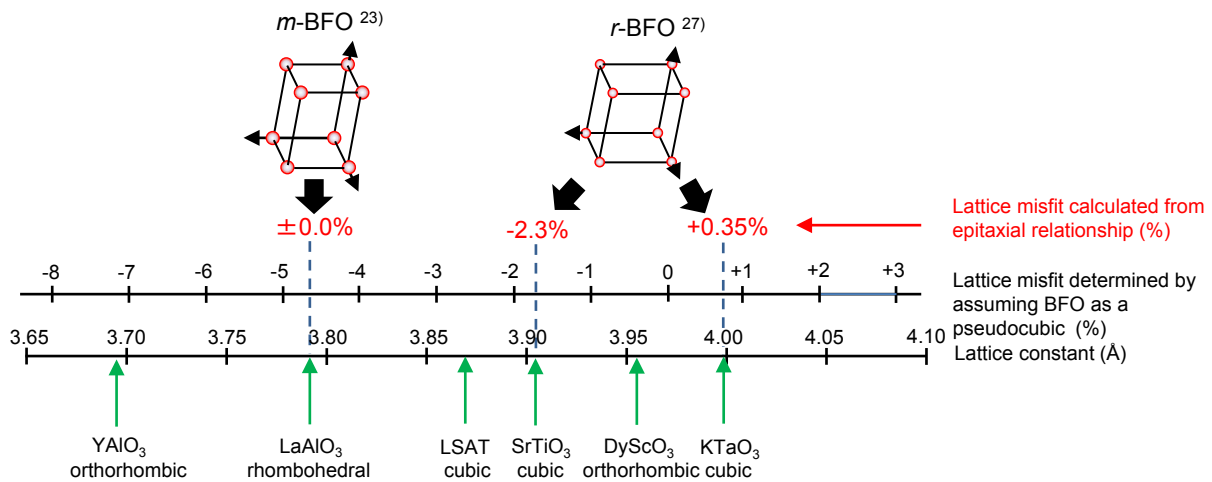
Now let us turn our attention to how the  $\sim 0.35\%$  biaxial strain applied along the in-plane direction could turn up along the out-of-plane direction. It is worth noting that although the transmission electron diffraction technique provides a wide range reciprocal lattice information which makes it advantageous over XRD for investigating crystalline symmetry, its accuracy is limited to  $\sim 2\%$  with Bragg's reflections in the zero-order Laue zone.<sup>36)</sup> On the other hand, XRD provides better resolution in a highly localized area in a reciprocal space. In addition, XRD data are volume-averaged over the entire BFO film, i.e., up to the  $\sim \text{mm}$  (or above  $\sim \text{mm}$ ) scale, which inherently ensures more signals than transmission electron diffraction data, which are obtained from a highly localized area, i.e., less than  $2\text{--}3\ \mu\text{m}$  typically. Thus, XRD is clearly advantageous over transmission electron diffraction in terms of the precise measurement of reciprocal lattice information from the entire volume of a BFO film.<sup>12)</sup>

Figure 17(c) shows an XRD  $\theta\text{--}2\theta$  scan along the surface normal, i.e., out-of-plane, direction. Note that the Bragg's



**Fig. 17.** (Color online) XRSM demonstrating the existence of  $(2\bar{1}\bar{3})_{\text{BFO}}$  reflection with (b) its intensity profile as a function of  $2\theta$ . (c) XRD with  $q\text{--}2q$  geometry, i.e., along surface normal orientation, demonstrating that the locations of  $(10\bar{2})_{\text{BFO}}$ ,  $(20\bar{4})_{\text{BFO}}$ , and  $(30\bar{6})_{\text{BFO}}$  Bragg's reflections appear at slightly higher  $2\theta$  angles than those of  $(100)_{\text{KTO}}$ ,  $(200)_{\text{KTO}}$ , and  $(300)_{\text{KTO}}$  Bragg's reflections. Reproduced from Ref. 12 with permission.

peak locations of  $(100)_{\text{KTO}}$ ,  $(200)_{\text{KTO}}$ , and  $(300)_{\text{KTO}}$  are  $2\theta = 22.28^\circ (= 0.3987\ \text{nm})$ ,  $45.44^\circ (= 0.1994\ \text{nm})$ , and  $70.80^\circ (= 0.1329\ \text{nm})$ , respectively. These match well with corresponding Bragg's peak locations of an unstrained KTO material.<sup>37)</sup> On the other hand, the Bragg's peak locations of  $(10\bar{2})_{\text{BFO}}$ ,  $(20\bar{4})_{\text{BFO}}$ , and  $(30\bar{6})_{\text{BFO}}$  in Fig. 17(c) are calculated to correspond to 0.3928, 0.1966, and 0.1311 nm, respectively. These lattice plane spacings are  $\sim 1.6\%$  smaller than 0.3994, 0.1997, and 0.1331 nm of the corresponding lattice plane spacings from unstrained r-BFO,<sup>35)</sup> indicating that the lattice plane spacing in BFO along the out-of-plane direction is decreased owing to the biaxial tensile stress along the in-plane direction. This leads to a Poisson's ratio of  $\sim 0.68$  determined using the equation  $\nu = \epsilon_{xx}/\epsilon_{zz}/(\epsilon_{zz}/\epsilon_{xx} - 2)$ , where  $\epsilon_{xx}$  and  $\epsilon_{zz}$  are the in-plane and out-of-plane lattice mismatches, respectively.<sup>38,39)</sup> This Poisson's ratio is slightly higher than  $\sim 0.49$  previously reported for BFO thin films.<sup>38)</sup> The discrepancy could be due to two factors: (1) the use of different BFO growth techniques, i.e., pulsed laser deposition (previous work) vs ultrahigh vacuum sputtering (current work) and (2) the presence of single-domain microstructure with less source of strain release (current work) vs multidomain microstructures with possibly more sources of strain release such as dislocations and grain boundaries (previous work). However, further study is necessary to elucidate this point.



**Fig. 18.** (Color online) Summary of BFO lattice misfit values calculated on the basis of the determined epitaxial relationship with LAO, STO, and KTO substrates (in red). BFO lattice misfit values, by assuming BFO as a pseudocubic are shown also (in black) for comparison. They clearly deviate from those derived from the epitaxial relationship study, indicating that epitaxial relationship investigation is required for precise lattice misfit evaluation.

In summary, the relationship between the substrate-induced biaxial strains and the subsequent crystal structures induced in BFO films grown using ultrahigh vacuum rf magnetron sputtering is illustrated in Fig. 18 in relation to other perovskite-based oxide materials. Note that the lattice misfit values estimated on the basis of conventional pseudocubic assumption of BFO (in black) deviate from the ones derived from the epitaxial relationships determined experimentally for STO, LAO, and KTO (in red). This clearly indicates that the precise measurement of the lattice misfit, i.e., lattice strain, within epitaxial BFO films requires the identification of the crystalline phase as well as the epitaxial relationship of the films with the substrate materials.

## 5. Conclusions

The precise crystal structure and strain measurement strategy for epitaxially grown BFO films are reviewed by using examples of BFO films grown with different thicknesses and substrates. The step-by-step procedure is as follows:

(1) To investigate overall crystal and microstructures in a BFO film, the combination of *multi-zone axes* transmission electron diffraction pattern analysis and structure factor calculations is required to confirm the *three-dimensional* structural characteristic within the BFO film. (This is particularly important owing to the remarkably complex nature of the BFO crystal structure as demonstrated, for instance, in Figs. 1, 2, and 4.)

(2) If the BFO film match none of the previously known phases, first-principles calculation (or other computational methods) may need to be implemented to provide an atomistic structural model of a new BFO phase for which the structure factor can be calculated. The structure factor calculation results should be compared with transmission electron diffraction patterns along multiple zone axes to ensure the validity of the atomistic structural model.

(3) The epitaxial relationship between the BFO film and the substrate needs to be subsequently constructed to accurately calculate the misfit strain at the BFO/substrate interface. XRD and XRSM can be used to accurately evaluate the lattice plane strain (and/or distortion) resulting from the biaxial strain imposed by the substrate if necessary.

It is concluded that TEM is highly effective in determining the overall crystal symmetry because this technique provides wide-area reciprocal space information, which is crucial to the proper evaluation of the *symmetry* that uniquely depends on the crystallographic details of BFO, i.e., space group, lattice parameter, and locations of all basis atoms in a unit cell. On the other hand, for the precise measurement of the lattice strain and possible variations within the symmetry, XRD is advantageous over TEM owing to its capability to measure a localized reciprocal space with superior precision. Thus, it is critically important to utilize both of the TEM and XRD techniques for the comprehensive structural analysis of epitaxial BFO films.

## Acknowledgements

This work was partially funded by Small Scale Systems Integration and Packaging Center (S<sup>3</sup>IP) at State University of New York at Binghamton. S<sup>3</sup>IP is a New York State Center of Excellence and receives funding from the New York State Office of Science, Technology and Innovation (NYSTAR), the Empire State Development Corporation, and a consortium of industrial members. This work was partly supported by a Grant-in-Aid for Scientific Research (Category B, No. 15H03548), and JSPS Fellows No. JP16J01892.

- 1) G. A. Smolenskii and I. E. Chupis, *Usp. Fiz. Nauk* **137**, 415 (1982).
- 2) S. V. Kiselev, R. P. Ozerov, and G. S. Zhdanov, *Sov. Phys. Dokl.* **7**, 742 (1963).
- 3) I. Sosnowska, T. Peterlin-Neumaier, and E. Steichele, *J. Phys. C* **15**, 4835 (1982).
- 4) J. R. Teague, R. Gerson, and W. J. James, *Solid State Commun.* **8**, 1073 (1970).
- 5) D. Lebeugle, D. Colson, A. Forget, and M. Viret, *Appl. Phys. Lett.* **91**, 022907 (2007).
- 6) D. Sando, A. Barthélémy, and M. Bibes, *J. Phys.: Condens. Matter* **26**, 473201 (2014).
- 7) D. G. Schlom, L.-Q. Chen, C.-B. Eom, K. M. Rabe, S. K. Streiffer, and J.-M. Triscone, *Annu. Rev. Mater. Res.* **37**, 589 (2007).
- 8) X. Qi, M. Wei, Y. Lin, Q. Jia, D. Zhi, J. Dho, M. G. Blamire, and J. L. MacManus-Driscoll, *Appl. Phys. Lett.* **86**, 071913 (2005).
- 9) H. Béa, M. Bibes, X.-H. Zhu, S. Fusil, K. Bouzehouan, S. Petit, J. Kreisel, and A. Barthélémy, *Appl. Phys. Lett.* **93**, 072901 (2008).

- 10) I.-T. Bae and H. Naganuma, *Appl. Phys. Express* **8**, 031501 (2015).
- 11) I.-T. Bae, H. Naganuma, T. Ichinose, and K. Sato, *Phys. Rev. B* **93**, 064115 (2016).
- 12) I.-T. Bae, T. Ichinose, M.-G. Han, Y. Zhu, S. Yasui, and H. Naganuma, *Sci. Rep.* **8**, 893 (2018).
- 13) D. Ricinchi, K. Y. Yun, and M. Okuyama, *J. Phys.: Condens. Matter* **18**, L97 (2006).
- 14) H. Béa, B. Dupe, S. Fusil, R. Mattana, E. Jacquet, B. Warot-Fonrose, F. Wilhelm, A. Rogalev, S. Petit, V. Cros, A. Anane, F. Petroff, K. Bouzouhouane, G. Geneste, B. Dkhil, S. Lisenkov, I. Ponomareva, L. Bellaiche, M. Bibes, and A. Barthélémy, *Phys. Rev. Lett.* **102**, 217603 (2009).
- 15) R. J. Zeches, M. D. Rossell, J. X. Zhang, A. J. Hatt, Q. He, C.-H. Yang, A. Kumar, C. H. Wang, A. Melville, C. Adamo, G. Sheng, Y.-H. Chu, J. F. Chu, J. F. Ihlefeld, R. Erni, C. Ederer, V. Gopalan, L. Q. Chen, D. G. Schlom, N. A. Spaldin, L. W. Martin, and R. Ramesh, *Science* **326**, 977 (2009).
- 16) Z. Chen, L. You, C. Huang, Y. Qi, J. Wang, T. Sritharan, and L. Chen, *Appl. Phys. Lett.* **96**, 252903 (2010).
- 17) H. M. Christen, J. H. Nam, H. S. Kim, A. J. Hatt, and N. A. Spaldin, *Phys. Rev. B* **83**, 144107 (2011).
- 18) J. C. Yang, Q. He, S. J. Suresh, C. Y. Kuo, C. Y. Peng, R. C. Haismaier, M. A. Motyka, G. Sheng, C. Adamo, H. J. Lin, Z. Hu, L. Chang, L. H. Tjeng, E. Arenholz, N. J. Podraza, M. Bernhagen, R. Uecker, D. G. Schlom, V. Gopalan, L. Q. Chen, C. T. Chen, R. Ramesh, and Y. H. Chu, *Phys. Rev. Lett.* **109**, 247606 (2012).
- 19) G. Xu, H. Hiraka, G. Shirane, J. Li, J. Wang, and D. Viehland, *Appl. Phys. Lett.* **86**, 182905 (2005).
- 20) H. Liu, K. Yao, P. Yang, Y. Du, Q. He, Y. Gu, X. Li, S. Wang, X. Zhou, and J. Wang, *Phys. Rev. B* **82**, 064108 (2010).
- 21) G. Xu, J. Li, and D. Viehland, *Appl. Phys. Lett.* **89**, 222901 (2006).
- 22) Z. Chen, Y. Qi, L. You, P. Yang, C. W. Huang, J. Wang, T. Sritharan, and L. Chen, *Phys. Rev. B* **88**, 054114 (2013).
- 23) I.-T. Bae, A. Kovacs, H. J. Zhao, J. Iniguez, S. Yasui, T. Ichinose, and H. Naganuma, *Sci. Rep.* **7**, 46498 (2017).
- 24) L. Yan, H. Cao, J. Li, and D. Viehland, *Appl. Phys. Lett.* **94**, 132901 (2009).
- 25) O. Diéguez, O. E. González-Vázquez, A. C. Wojdel, and J. Íñiguez, *Phys. Rev. B* **83**, 094105 (2011).
- 26) D. Sando, B. Xu, L. Bellaiche, and V. Nagarajan, *Appl. Phys. Rev.* **3**, 011106 (2016).
- 27) F. Kubel and H. Schmid, *Acta Crystallogr., Sect. B* **46**, 698 (1990).
- 28) D. G. Schlom, L.-Q. Chen, C. J. Fennie, V. Gopalan, D. A. Muller, X. Pan, R. Ramesh, and R. Uecker, *MRS Bull.* **39**, 118 (2014).
- 29) M. Ishimaru, I.-T. Bae, Y. Hirotsu, S. Matsumura, and K. E. Sickafus, *Phys. Rev. Lett.* **89**, 055502 (2002).
- 30) I.-T. Bae, M. Ishimaru, Y. Hirotsu, and K. E. Sickafus, *J. Appl. Phys.* **96**, 1451 (2004).
- 31) I.-T. Bae and H. Naganuma, private communication.
- 32) I. C. Infante, J. Juraszek, S. Fusil, B. Dupé, P. Gemeiner, O. Diéguez, F. Pailloux, S. Jouen, E. Jacquet, G. Geneste, J. Pacaud, J. Íñiguez, L. Bellaiche, A. Barthélémy, B. Dkhil, and M. Bibes, *Phys. Rev. Lett.* **107**, 237601 (2011).
- 33) M. D. Rossell, R. Erni, M. P. Prange, J.-C. Idrobo, W. Luo, R. J. Zeches, S. T. Pantelides, and R. Ramesh, *Phys. Rev. Lett.* **108**, 047601 (2012).
- 34) F. Pailloux, M. Couillard, S. Fusil, F. Bruno, W. Saidi, V. Garcia, C. Carrétéro, E. Jacquet, M. Bibe, A. Barthélémy, G. A. Botton, and J. Pacaud, *Phys. Rev. B* **89**, 104106 (2014).
- 35) A. Palewicz, R. Przenioslo, I. Sosnowska, and A. W. Hewat, *Acta Crystallogr., Sect. B* **63**, 537 (2007).
- 36) D. B. Williams and C. B. Carter, *Transmission Electron Microscopy* (Springer, Boston, MA, 2009) 2nd ed., Chap. 21.
- 37) H. F. McMurdie, M. C. Morris, E. H. Evans, B. Paretzkin, W. Wong-Ng, Y. Zhang, and C. R. Hubbard, *Powder Diffr.* **2**, 41 (1987).
- 38) Z. Chen, Z. Luo, C. Huang, Y. Qi, P. Yang, L. You, C. Hu, T. Wu, J. Wang, C. Gao, T. Sritharan, and L. Chen, *Adv. Funct. Mater.* **21**, 133 (2011).
- 39) A. Kossov, E. Wachtel, and I. Lubmirsky, *J. Electroceram.* **32**, 47 (2014).